JM PAPERS

Flow state transition induced by emergence of orbiting satellite eddies in two-dimensional turbulent Rayleigh–Bénard convection

Zhen-Yuan Gao[1],[‡], Xin Tao[2],[‡], Shi-Di Huang[1],[3],[†], Yun Bao[4] and Yi-Chao Xie[2],[†]

[1]Center for Complex Flows and Soft Matter Research and Department of Mechanics and Aerospace Engineering, Southern University of Science and Technology, Shenzhen 518055, PR China

[2]State Key Laboratory for Strength and Vibration of Mechanical Structures and School of Aerospace, Xi'an Jiaotong University, Xi'an 710049, PR China

[3]Guangdong Provincial Key Laboratory of Turbulence Research and Applications, Southern University of Science and Technology, Shenzhen 518055, PR China

[4]School of Aeronautics and Astronautics, Sun Yat-sen University, Shenzhen 518107, PR China

We report a numerical investigation of a previously noticed but less explored flow state transition in two-dimensional turbulent Rayleigh–Bénard convection. The simulations are performed in a square domain over a Rayleigh number range of $10^7 \leq Ra \leq 2 \times 10^{11}$ and a Prandtl number range of $0.25 \leq Pr \leq 20$. The transition is characterized by the emergence of multiple satellite eddies with increasing Ra, which orbit around and interact with the main vortex roll in the system. Consequently, the main roll is squeezed to a smaller size compared with the domain and wanders around in the bulk region irregularly and extensively. This is in sharp contrast to the flow state before the transition, which is featured by a domain-sized circulatory roll with its vortex centre 'condensed' near the domain's centre. Detailed velocity field analysis reveals that there exists an abrupt increase in the energy fluctuations of the Fourier modes during the transition. Based on this phase-transition-like signal, the critical condition for the transition is found to follow a scaling relation as $Ra_t \sim Pr^{1.41}$ where Ra_t is the critical Rayleigh number for the transition. This scaling relation is quantitatively explained by a phenomenological model grounded on the bistability behaviour (i.e. spontaneous and stochastic switching between the two flow states) observed at the edge of the transition. The model can also account for the effects of aspect ratio on the transition reported in the literature (van der Poel *et al.*, *Phys. Fluids*, vol. 24, 2012).

Key words: Bénard convection, turbulent convection

† Email addresses for correspondence: huangsd@sustech.edu.cn, yichao.xie@xjtu.edu.cn
‡ Z.-Y.G. and X.T. contributed equally to this work.

1. Introduction

Turbulent thermal convection is ubiquitous in nature and engineering applications. Examples include thermal convection in the solar convection zone (Cattaneo, Emonet & Weiss 2003), in the atmosphere (Hartmann, Moy & Fu 2001) and in the metal-production processes (Brent, Voller & Reid 1988). Rayleigh–Bénard convection (RBC), a fluid layer heated from below and cooled from above, is an ideal system for studying the general mechanism of thermal convection (for reviews, see Ahlers, Grossmann & Lohse 2009; Lohse & Xia 2010; Chillà & Schumacher 2012; Xia 2013). For a given geometry, the RBC system is controlled by two dimensionless parameters, namely, the Rayleigh number Ra measuring the strength of the thermal driving and the Prandtl number Pr characterizing the relative diffusion of momentum and heat.

A salient feature of RBC is the existence of a domain-sized circulatory roll, known as the large-scale circulation (LSC) or the 'wind of turbulence' in the literature, which appears when the Ra number is sufficiently large. Thanks to its rich intriguing dynamics, the LSC has been studied extensively over the years. These studies include its formation and evolution processes (e.g. Xi, Lam & Xia 2004; Li *et al.* 2021; Wei 2021; Ren *et al.* 2022); its spatial-temporal motion, such as the azimuthal meandering, the periodic twisting and sloshing oscillation, and the recently discovered jump rope mode (e.g. Ciliberto, Cioni & Laroche 1996; Qiu, Yao & Tong 2000; Funfschilling, Brown & Ahlers 2008; Xi *et al.* 2009; Zhou *et al.* 2009; Yanagisawa *et al.* 2010; Vogt *et al.* 2018; Li *et al.* 2022); its sudden change in flow structure and dynamics, such as cessation, reorientation and reversal (e.g. Brown, Nikolaenko & Ahlers 2005; Brown & Ahlers 2006; Xi & Xia 2007; Xie, Wei & Xia 2013; Chen *et al.* 2019); and the flow mode transition (e.g. Xi & Xia 2008; Zwirner, Tilgner & Shishkina 2020; Chen *et al.* 2023). One important message learnt from these studies is that, while the LSC dynamics is three dimensional, its geometric structure is mostly quasi two dimensional.

The quasi-two-dimensional (quasi-2-D) character of the LSC has motivated researchers to employ 2-D geometry to investigate its behaviours by means of direct numerical simulations (DNS) (Sugiyama *et al.* 2009, 2010), as it is more feasible to get long-term statistics over a wide parameter space. Although 2-D DNS cannot reflect the complex flow dynamics in three-dimensional (3-D) systems, it has been shown that 2-D and 3-D RBCs share many similarities in flow morphology and global properties, in particular when Pr is large (Schmalzl, Breuer & Hansen 2004; van der Poel, Stevens & Lohse 2013; He *et al.* 2021; Li *et al.* 2021). Moreover, the Grossmann–Lohse model based on 2-D boundary-layer equations has achieved great success in predicting heat transfer behaviours in 3-D turbulent RBC (Grossmann & Lohse 2000, 2001; Stevens *et al.* 2013). These findings suggest that 2-D RBC can be utilized as an efficient approach to shed light on the physics of its 3-D counterpart.

Indeed, fruitful 2-D studies over the past decade have improved our understanding of turbulent RBC in various aspects. These aspects are not limited to the LSC *per se* (e.g. Chandra & Verma 2011; Podvin & Sergent 2015; Castillo-Castellanos *et al.* 2019; Wang *et al.* 2020; Xu, Chen & Xi 2021), but also include the heat transport behaviours (e.g. van der Poel, Stevens & Lohse 2011; Huang & Zhou 2013; Zhu *et al.* 2018; Zhang & Zhou 2024), the structure and dynamics of boundary layers (e.g. Zhou *et al.* 2010; van der Poel *et al.* 2015; Pandey 2021) and small-scale statistics of turbulence (e.g. Zhang, Zhou & Sun 2017; Xie & Huang 2022; He, Bao & Chen 2023; Samuel & Verma 2024). Despite the diverse topics, a common phenomenon can be noticed (but less mentioned) from the instantaneous flow fields shown in most of these studies on 2-D turbulent RBC:

the domain-sized LSC breaks up and is replaced by several vortices of smaller sizes under certain conditions.

This phenomenon was first reported by van der Poel *et al.* (2012), where they termed the flow field dominated by a LSC of domain size as the condensed state, and that featured by several vortices of smaller sizes as the uncondensed state. Although the two distinct flow states are visible in many studies of 2-D RBC mentioned above, this transition has received less attention before. To the best of our knowledge, the two relevant studies mainly focused on how the heat transport behaviours in 2-D RBC are connected to different flow states (van der Poel *et al.* 2012; Labarre, Fauve & Chibbaro 2023). Specifically, based on a sudden change in the heat transfer efficiency at $Pr = 1$, van der Poel *et al.* (2012) found that a transitional Rayleigh number Ra_t scales with the aspect ratio Γ (the width-to-height ratio of the domain) as $Ra_t \sim \Gamma^{-2.44}$ in the range of $0.23 \leq \Gamma \leq 2/3$, which becomes almost Γ independent for $\Gamma = 1$ and 2. Recently, Labarre *et al.* (2023) reported that heat-flux fluctuation is more sensitive to the change in flow state and the transition occurs at $Ra_t/Pr \approx 10^9$ for $Pr = 0.71$ and 7.

However, the above two studies were conducted in limited parameter ranges. It remains unclear how the flow state transition occurs quantitatively and what determines the critical condition for Ra_t. Since how the flow structure evolves with increasing Ra and Pr is an important issue in the studies of turbulent RBC, it deserves to carry out an in-depth investigation of this transition and unravel its mechanism. The knowledge gained from the study in 2-D RBC could stimulate further studies in quasi-2-D turbulent RBC, as we shall discuss in the conclusion of this paper. In addition, similar transitions in flow topology can be observed in various turbulence systems (e.g. Weeks *et al.* 1997; Bouchet & Simonnet 2009; Huisman *et al.* 2014; Xie, Ding & Xia 2018; Favier, Guervilly & Knobloch 2019; Yang *et al.* 2020). A systematic investigation of the present transition may also provide new insights into similar phenomena in other systems.

In the present study, by conducting extensive DNS of 2-D turbulent RBC over a wide parameter space (see figure 1) and quantifying the flow field in detail, we found that the critical condition for the flow state transition follows a scaling relation as $Ra_t = 1.1 \times 10^9 Pr^{1.41}$, rather than $Ra_t/Pr \approx 10^9$ reported by Labarre *et al.* (2023) based on only two values of Pr. By examining the spontaneous switching processes between the two flow states, which are observed in the vicinity of Ra_t, we reveal that the critical condition for the transition is set by the balance between the typical travel time of thermal plumes (the elementary flow structures in RBC) and their typical dissipation time in the flow. This physical picture not only gives a prediction in good agreement with the Ra_t-Pr scaling found in the present study, but also explains the effect of aspect ratio on the aforementioned transition reported by van der Poel *et al.* (2012).

The remainder of this paper is organized as follows. We first introduce details of the numerical simulations in § 2. Then we show in § 3.1 how the flow pattern and dynamics are changed before and after the flow state transition. These changes are further quantified by Fourier mode analysis in § 3.2, based on which we obtain the Ra_t-Pr dependence for the transition. The mechanism that determines this transition is revealed in § 3.3 by examining the flow states in the vicinity of Ra_t. The main findings of the present study are summarized in § 4, where we also discuss the implication of the present phenomenon to quasi-2-D RBC and its similarity to the flow transitions in other turbulence systems.

2. The numerical set-up

We consider a 2-D RBC system in a square domain with no-slip and impermeable velocity boundary conditions for all walls. The temperature boundary conditions for the sidewalls
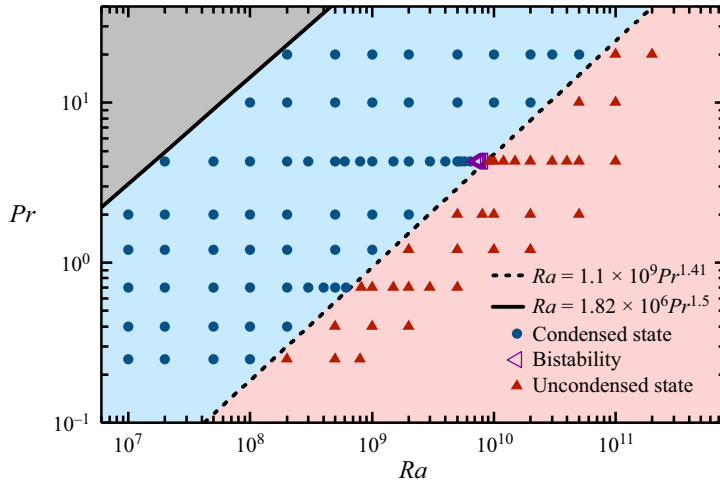
Figure 1. A *Ra-Pr* phase diagram showing all parameters explored in the present study. The grey region is the flow regime without a LSC and its boundary is given by the solid line (Grossmann & Lohse 2000). The blue and red regions are the flow regimes characterized by the condensed state (solid circles) and the uncondensed state (solid triangles), respectively, which are separated by the dashed line $Ra_t = 1.1 \times 10^9 Pr^{1.41}$ determined in § 3.2. The open triangles highlight the *Ra* range (from $Ra = 7.15 \times 10^9$ to $Ra = 8.10 \times 10^9$) with bistable states observed at $Pr = 4.3$. This bistability behaviour will be discussed in § 3.3.

are adiabatic, while those for the top and bottom walls are isothermal. By employing the Oberbeck–Boussinesq approximation and the linear equation of state (Landau & Lifshitz 1987), the dimensionless governing equations for this system are

$$\nabla \cdot \boldsymbol{u} = 0, \tag{2.1}$$

$$\frac{\partial \boldsymbol{u}}{\partial t} + (\boldsymbol{u} \cdot \nabla)\boldsymbol{u} = -\nabla p + \sqrt{\frac{Pr}{Ra}}\nabla^2 \boldsymbol{u} + T\hat{\boldsymbol{e}}_z, \tag{2.2}$$

$$\frac{\partial T}{\partial t} + (\boldsymbol{u} \cdot \nabla)T = \frac{1}{\sqrt{RaPr}}\nabla^2 T, \tag{2.3}$$

where $\boldsymbol{u} = (u_x, u_z)$, T and p are, respectively, the dimensionless velocity, temperature and pressure fields; $\hat{\boldsymbol{e}}_z$ is the unit vector antiparallel to gravity. The $Ra = \alpha g \Delta T H^3/(\nu\kappa)$ and $Pr = \nu/\kappa$ numbers in these equations are the two control parameters of the system. Here, H is the domain's height; ΔT is the imposed temperature difference between the top and bottom walls; g is the gravitational acceleration; α, ν and κ are the isobaric thermal expansion coefficient, the kinematic viscosity and the thermal diffusivity of the working fluid, respectively. The control parameters explored in the present study are shown in figure 1 (a total of 109 cases), covering four decades in the *Ra* number and almost two decades in the *Pr* number. To better capture the transition process, more *Ra* numbers were simulated in the vicinity of the transition for $Pr = 4.3$.

We solved (2.1)–(2.3) by employing a numerical code (Bao, Luo & Ye 2018) that has been used in a previous study of turbulent RBC (Bao *et al.* 2015). This code applies a second-order central difference for the spatial discretization and a second-order Runge–Kutta scheme for the time marching. To resolve the smallest length scale in the flow, i.e. the Kolmogorov scale η_K when $Pr \leq 1$ or the Bachelor scale η_B when $Pr > 1$, the maximal grid sizes Δ_g are set to be smaller than η_K or η_B. Moreover, the grid points used for resolving the boundary layer are typically four times larger than the requirements proposed by Shishkina *et al.* (2010). The time steps are also small enough so that the
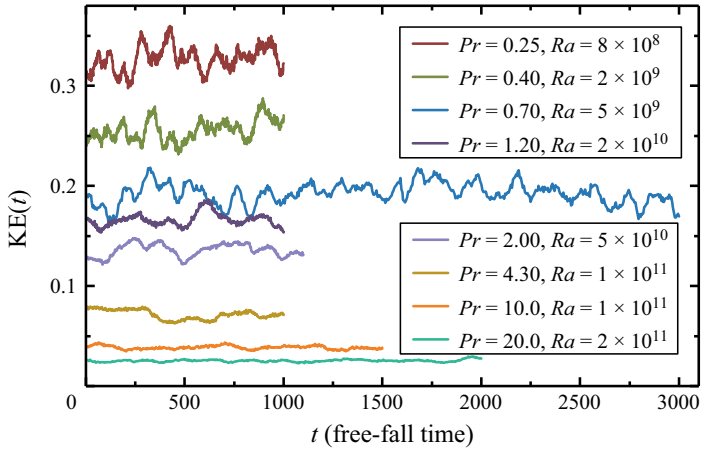
Figure 2. Time traces of the kinetic energy of the whole flow in the stationary state. The data at the highest *Ra* for each *Pr* are shown as examples.

Courant–Friedrichs–Lewy numbers are smaller than 0.1 for all the cases. Details of the grid setting used for each simulation are provided in table 1 of the Appendix.

To avoid the potential influence of initial conditions, all the simulations were started with the same flow field being $\boldsymbol{u} = (0, 0)$ and $T = 0$. After the flow had reached the stationary state, we kept running the simulations for at least 1000 free-fall times to get statistics. According to a recent study (Lindborg 2023), the numerical convergence of 2-D RBC is very slow due to the inverse energy cascade, with the convergence time scale proportional to $\sqrt{Ra/Pr}$. For example, the computational time required for the convergence of the kinetic energy at $Pr = 1$ is approximately 1000 free-fall times at $Ra = 1 \times 10^{10}$, which increases to 3000 free-fall times at $Ra = 1 \times 10^{11}$. To check the convergence of our simulations, we plot in figure 2 the time traces of the kinetic energy of the whole flow in the stationary state at the highest *Ra* for each *Pr*. These parameters require the most computational time for convergence, but the corresponding data display no tendency to increase over time, indicating good convergence of our simulations.

The reliability of our simulations has been checked by comparing the values of the Nusselt number *Nu* (dimensionless heat transfer efficiency) obtained by three different methods: $Nu = \sqrt{RaPr}\langle u_z T \rangle_{V,t} + 1$ calculated from the definition; $Nu_{\epsilon_\theta} = \sqrt{RaPr}\langle \epsilon_\theta \rangle_{V,t}$ based on the thermal energy dissipation rate ϵ_θ; and $Nu_{\epsilon_u} = \sqrt{RaPr}\langle \epsilon_u \rangle_{V,t} + 1$ based on the kinetic energy dissipation rate ϵ_u. Here $\langle \cdot \rangle_{V,t}$ represents averaging over space and time. It is found that the relative differences between *Nu* and Nu_{ϵ_θ} (Nu_{ϵ_u}) are less than 1 % (3 %) for most of the cases (see table 1 in the Appendix). In addition, we have checked the statistical convergence by comparing the time-averaged values of *Nu* over the first and the last halves of each simulation, the relative difference of which is smaller than 1 % for all the cases in the present study. These validations suggest that the present simulations are reliable.

The accuracy of our simulations is further confirmed by comparing the compensated *Nu* shown in figure 3. It is seen that our data are in good agreement with those obtained in previous studies (Huang & Zhou 2013; van der Poel *et al.* 2013; Zhang *et al.* 2017; Labarre *et al.* 2023). It is worth noting that there exist some discrepancies between different studies at $Ra \simeq 10^9$ for $Pr = 0.70$ and $Ra \simeq 10^{10}$ for $Pr = 4.30$, which could be attributed to the bistability behaviour (van der Poel *et al.* 2012). This behaviour will be discussed in § 3.3.
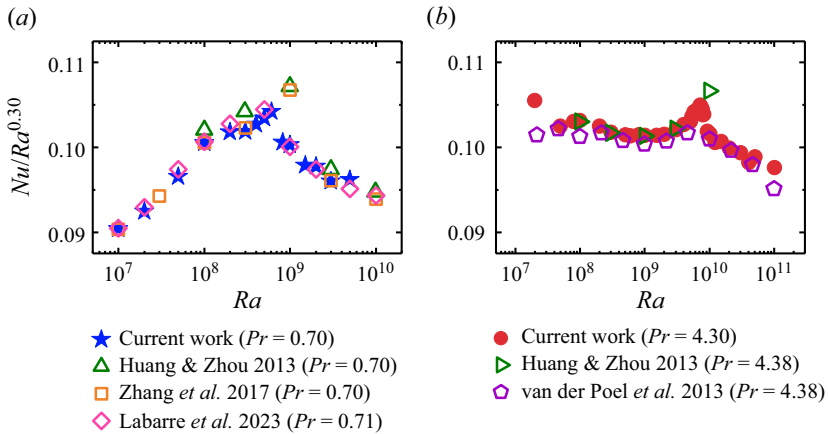
Figure 3. Plots of Nu compensated by $Ra^{0.30}$ as a function of Ra obtained in the present study (indicated by solid symbols): (*a*) $Pr = 0.70$ and (*b*) $Pr = 4.30$. The results obtained in previous studies (indicated by open symbols) at similar Pr are plotted together for comparison.
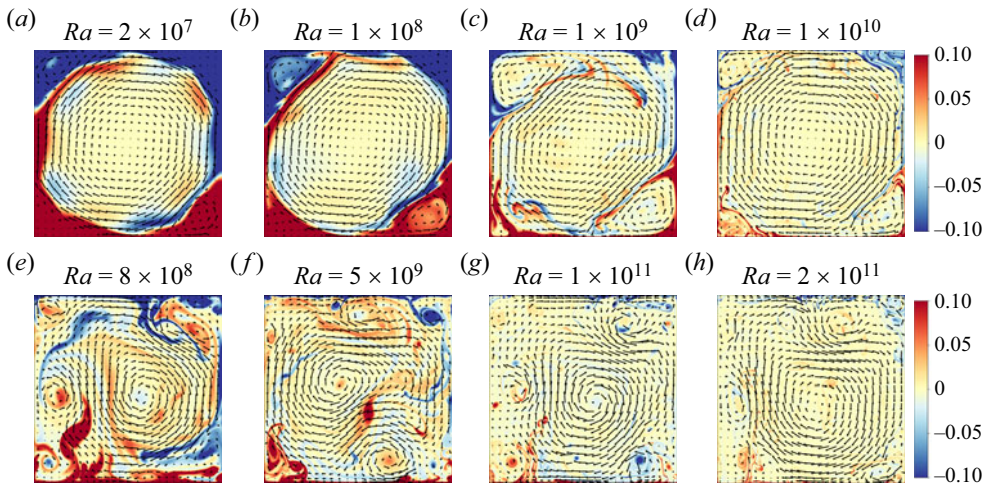

Figure 4. Instantaneous velocity–temperature fields for (*a*–*d*) the condensed state and (*e*–*h*) the uncondensed state for different Pr: (*a*,*e*) $Pr = 0.25$, (*b*,*f*) $Pr = 0.7$, (*c*,*g*) $Pr = 4.3$ and (*d*,*h*) $Pr = 20$. The velocity is coded by the length and orientation of the vector, and the temperature is colour coded with red (blue) representing hot (cold) fluid. The Ra number for each flow state is indicated on top of each subplot.

3. Results and discussion

3.1. *Flow states before and after the transition*

We first present how the flow pattern and dynamics are different before and after the flow state transition. Figure 4 shows typical snapshots of the flow field at two different Ra for each of the four selected Pr. For the cases with smaller Ra (the top panel of figure 4), the flow patterns for different Pr are all characterized by a domain-sized circulatory roll (i.e. the LSC known in the literature) and counter-circulating rolls in the corners, which are similar to those observed in quasi-2-D rectangular convection cells (e.g. Sugiyama *et al.* 2010; Chen *et al.* 2019). Although the LSC keeps changing its morphology with increasing Pr, which evolves from a circular shape at $Pr = 0.25$ to a tilted elliptical
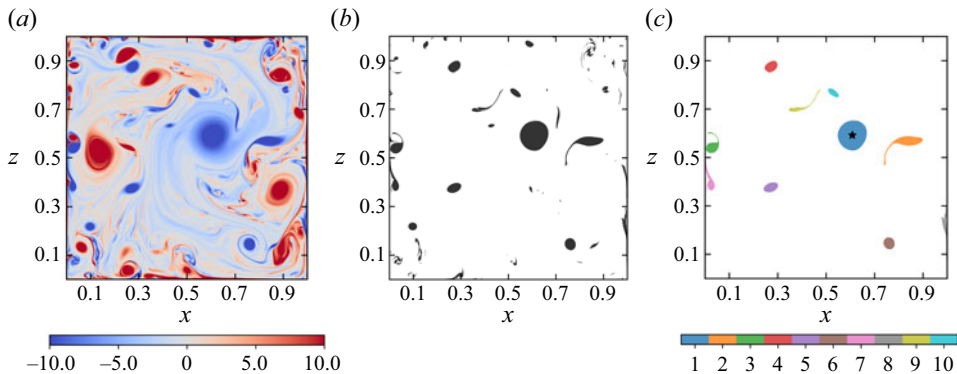
997 A54-6

Figure 5. Illustration of how to identify the vortex centre of the largest roll from the flow field. (*a*) A snapshot of the original vorticity field at $Pr = 4.3$ and $Ra = 1 \times 10^{11}$. The vorticity is colour coded with blue (red) representing clockwise (anti-clockwise) rotating vortices. (*b*) The identified vortices after applying a filtered threshold of $\omega < -8$ to the vorticity field in (*a*). (*c*) The vortices in (*b*) are sorted by their sizes and labelled with different colours. The star indicates the identified vortex centre of the largest roll. Note that different thresholds (ranging from $\omega < -4$ to $\omega < -12$) have been tested for this case and they have little impact on the result.

shape at $Pr = 4.3$ and recovers to a quasi-circular shape at $Pr = 20$, it can maintain at a stable state over tens of turnover time for all these cases. In addition, thermal plumes emitted from the top/bottom thermal boundary layers mostly follow the LSC's motion and move along the periphery region of the domain. In contrast, for the cases with larger Ra (figure 4*e–h*), no stable LSC of domain size can be seen any more. Instead, one observes a main circulatory roll smaller than the domain and several satellite eddies orbit around it. Due to the squeezing from these satellite eddies, the main roll is unstable and wanders in the bulk region irregularly. Moreover, some thermal plumes can survive and travel through the strongly turbulent bulk region for a long time. As a result, the flow field becomes more fluctuating and disordered. These dramatic changes in flow patterns and dynamics can be seen clearly in the supplementary movies available at https://doi.org/10.1017/jfm.2024.847.

The change from a stable LSC to an unstable main roll can be characterized by the motions of their vortex centres. To do so, we first identify the largest roll from the instantaneous flow field. This is achieved by filtering the vorticity field $\omega = \nabla \times \boldsymbol{u}(\boldsymbol{x}, t)$ with appropriate thresholds for different Ra and Pr numbers. The basic requirement to determine the threshold is that, after applying the threshold to the original vorticity field, the vortices with strong vorticities should be well distinguished and then extracted from the background flow. Taking the case with $Pr = 4.3$ and $Ra = 1 \times 10^{11}$ as an example, figure 5(*a*) shows that the flow is abundant of vortices with different sizes and strengths. By applying a threshold of $\omega < -8$ to the original vorticity field, the strong clockwise-rotating vortices, including the largest roll in the system, are identified (see figure 5*b*). These vortices were further sorted by their sizes and labelled with different colours. Then the centroid of the first labelled vortex is determined as the vortex centre of the largest roll, as indicated by a star in figure 5(*c*). As demonstrated in the supplementary movie, this method allows us to track the motion of the largest roll nicely.

The thus-determined trajectories of the vortex centre of the largest roll in different flow states are plotted in figure 6. It is seen that the vortex centre of the largest roll before the transition always stays near the domain's centre; in other words, its trajectory is 'condensed' in a limited area. By contrast, the vortex centre of the largest roll after the transition exhibits irregular motion and can explore the domain extensively; thus, its
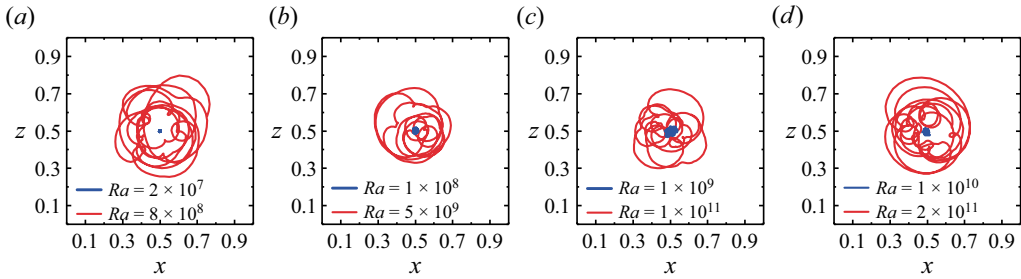
Figure 6. The trajectories of the vortex centre of the largest roll in the condensed state (blue) and the uncondensed state (red) for different Pr: (a) $Pr = 0.25$, (b) $Pr = 0.70$, (c) $Pr = 4.3$ and (d) $Pr = 20.0$. The Ra number for each flow state is indicated in the subplots.

trajectory is 'uncondensed'. Note that no appreciable sign of periodicity could be found by examining the autocorrelation functions of these trajectories, differing from the obvious periodically orbiting motion observed in a cylindrical cell of $\Gamma = 2$ by Li *et al.* (2022). Based on the distinct features of these trajectories, we term the flow states before and after the transition as the condensed and uncondensed states, respectively. It is worth noting that this terminology is the same as that in a previous study but from a different perspective (van der Poel *et al.* 2012). Here, we focus on the dynamics of the largest roll, while van der Poel *et al.* (2012) adopted the notation of condensation in 2-D turbulence (Kraichnan 1967; Xia *et al.* 2011) in the sense that the energy is piled up to a scale of the domain size in the condensed state, whereas the largest roll in the uncondensed state is smaller than the system scale. However, as the energy cascade of RBC is always contaminated by the walls and other complicating factors (Xie & Huang 2022), whether the present phenomenon could be understood by 2-D turbulence theory, which assumes homogeneity and isotropy of the flow, remains elusive and is outside the scope of this study.

3.2. *Determination of the transitional Rayleigh number Ra_t*

In addition to the change in the largest roll, another important feature of the flow state transition is the emergence of multiple satellite eddies with different sizes. This multi-scale feature could be captured by employing the Fourier mode analysis, which has been demonstrated as an efficient tool in previous studies of 2-D turbulent RBC (Chandra & Verma 2011; Wang *et al.* 2018; Xu *et al.* 2021). Specifically, the instantaneous velocity fields are projected onto the Fourier basis as below:

$$u_x(x, z, t) = \sum_{m,n} \hat{u}_x(m, n, t)[2\sin(m\pi x)\cos(n\pi z)], \tag{3.1}$$

$$u_z(x, z, t) = \sum_{m,n} \hat{u}_z(m, n, t)[-2\cos(m\pi x)\sin(n\pi z)]. \tag{3.2}$$

Here, $\hat{u}_i(m, n, t)$ $(i = x, z)$ is the amplitude of the (m, n) mode in the i direction at time instant t, and the corresponding energy contained in the (m, n) mode is $E^{m,n}(t) = |\hat{u}_x(m, n, t)|^2 + |\hat{u}_z(m, n, t)|^2$. Note that we have analysed the data by other methods such as proper orthogonal decomposition (Podvin & Sergent 2015; Xu *et al.* 2021). The results obtained are similar and the findings below are unaffected.

We first take the results obtained at $Pr = 4.3$ as an example for discussion. Figure 7(a,b) shows the time traces of the normalized energy contained in the first nine Fourier modes
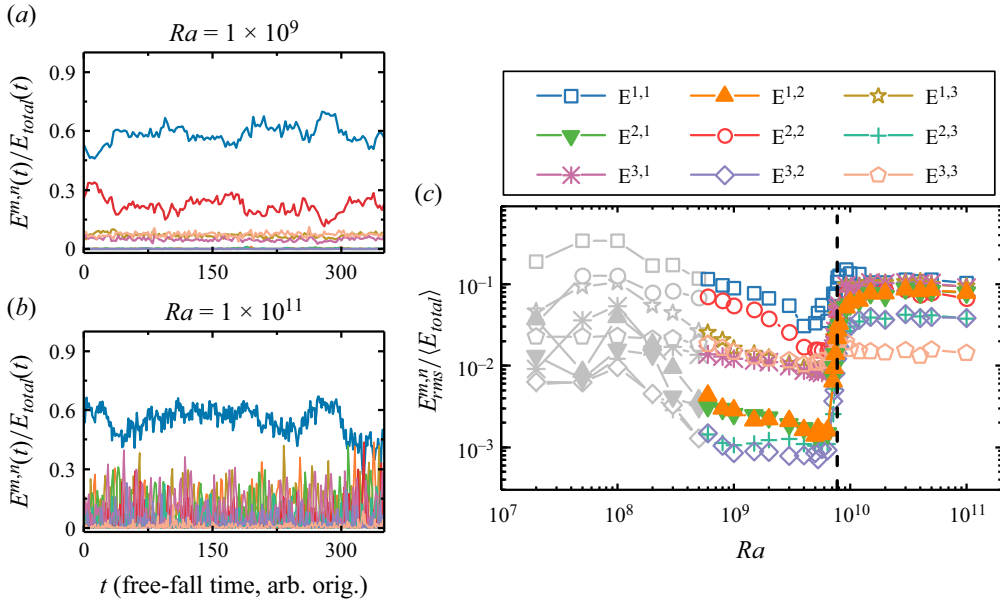
997 A54-8

Figure 7. Time traces of the energy contained in the first nine Fourier modes $E^{m,n}$ normalized by the total energy of all modes E_{total} at $Pr = 4.3$: (*a*) an example in the condensed state and (*b*) an example in the uncondensed state. (*c*) The normalized r.m.s. values of $E^{m,n}$ as a function of Ra at $Pr = 4.3$. The vertical dashed line indicates the location of the transitional Ra number Ra_t. The grey symbols represent the cases with LSC reversals, which is consistent with the finding by Sugiyama *et al.* (2010).

$E^{m,n}$ (i.e. m and $n = 1, 2, 3$) before and after the flow state transition. Here $E_{total}(t)$ represents the total energy of all Fourier modes at time instant t. It is seen that the system is dominated by the (1,1) and (2,2) modes before the transition, corresponding to the LSC and the corner rolls observed in the condensed state, respectively. Although the contributions from some other modes are also visible, their fluctuations in time are relatively gentle. When it goes to the uncondensed state, the (1,1) mode is still prevailing but becomes more fluctuating, consistent with the observation that the largest roll is unstable in this state. More importantly, vigorous fluctuations can be seen in the time traces of the normalized energy for almost all modes after the transition. This is in particular for the (1,2) and (2,1) modes, which are activated pronouncedly in the uncondensed state, in contrast to their negligible energies and fluctuations in the condensed case. As the (1,2) or (2,1) mode represents a flow structure with two horizontally or vertically stacked rolls, their activation could be attributed to the emergence of the satellite eddies that orbit around the main roll. It is their orbiting motions and interaction with the main roll that lead to the vigorous fluctuations observed here.

   To quantify how the energy fluctuations of different Fourier modes change during the transition, we plot their root-mean-square (r.m.s.) values $E^{m,n}_{rms}$ as a function of Ra in figure 7(*c*). Here, $E^{m,n}_{rms}$ is normalized by the time-averaged total energy of all Fourier modes $\langle E_{total} \rangle$. The grey symbols represent that LSC reversals can be observed for these cases, which makes the Ra dependence of $E^{m,n}_{rms}/\langle E_{total} \rangle$ complicated. For $Ra > 4 \times 10^8$ without LSC reversals, the data first decreases with Ra gradually and then jumps up abruptly at a transitional Ra number Ra_t for all modes. Visual inspection of the flow field confirms that it is in the vicinity of Ra_t that the flow state transition occurs. Therefore, the abrupt change in $E^{m,n}_{rms}/\langle E_{total} \rangle$ can be used as an indicator of the transition. Since
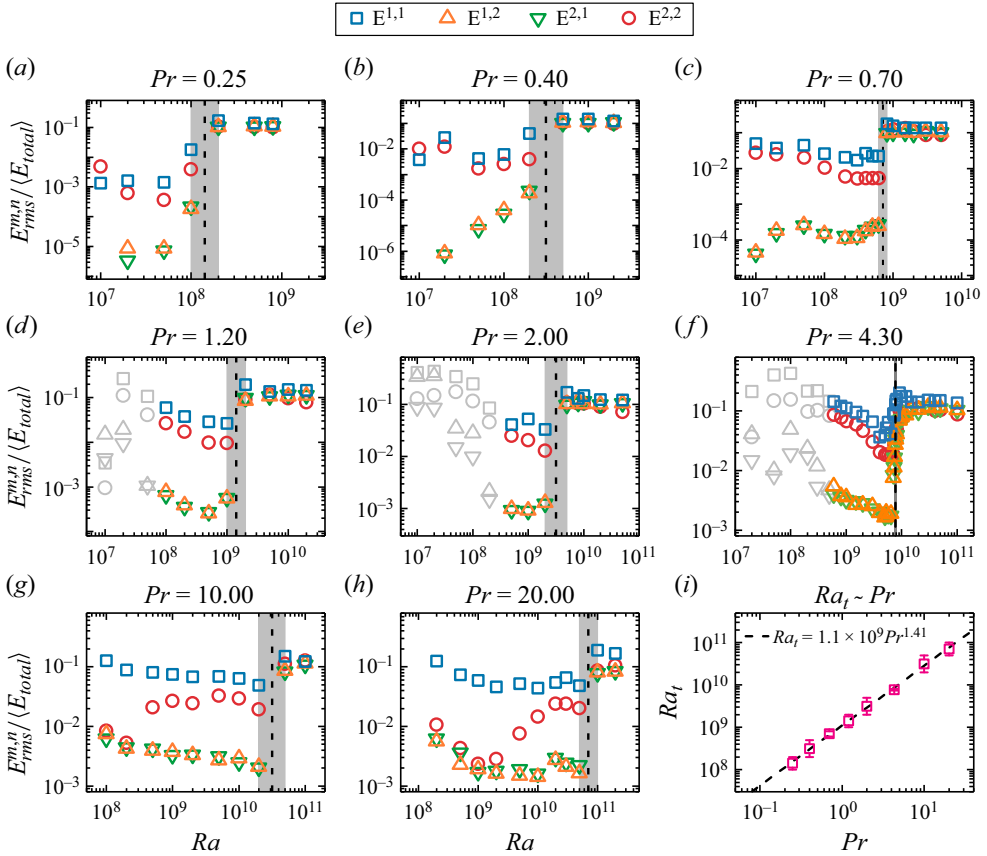
Figure 8. (*a–h*) The normalized r.m.s.values of the energy contained in the Fourier modes as a function of *Ra* for different *Pr*. Only the first four modes are shown for the clarity of presentation, as they are sufficient to reveal the transition behaviour. The vertical dashed line indicates the location of Ra_t with the uncertainty marked by the shaded region. The grey symbols represent the cases with LSC reversals, which is consistent with the *Ra-Pr* phase diagram of LSC reversals reported by Sugiyama *et al.* (2010), further illustrating the reliability of our simulations. (*i*) Plot of Ra_t as a function of *Pr*. The error bar represents the shaded region in (*a–h*). The dashed line is a power law fit to the data.

such a jump is most significant in the (1,2) and (2,1) modes, the value of Ra_t can be determined by finding the location of the maximum growth rate of $E_{rms}^{1,2}$ or $E_{rms}^{2,1}$, which yields $Ra_t = 7.7 \times 10^9$ for $Pr = 4.3$.

The above-discussed abrupt change in the energy fluctuations of Fourier modes can be found for all *Pr* explored in the present study. As shown in figure 8(*a–h*), although the detailed *Ra*-dependent trends of $E_{rms}^{m,n}/\langle E_{total}\rangle$ are different for different *Pr*, the (1,2) and (2,1) modes exhibit a similar sharp jump for all the cases. However, due to the unaffordable cost of running massive simulations near Ra_t for all *Pr*, we did not determine the values of Ra_t for other *Pr* using the same method as that for $Pr = 4.3$. Instead, we first locate the *Ra* range where $E_{rms}^{1,2}$ (or $E_{rms}^{2,1}$) shows an abrupt increase, and then estimate Ra_t as the average value of the two *Ra* numbers just before and after this increase. The so-obtained Ra_t is indicated by the dashed line in each subplot of figure 8(*a–h*), with its uncertainty represented by the shaded region. Quantitatively, one sees in figure 8(*i*) that Ra_t increases with *Pr* and can be fitted by a power law as $Ra_t = 1.1 \times 10^9 Pr^{1.41\pm0.02}$. This scaling

997 A54-10

Figure 9. Time traces of (*a*) *Nu* and (*b*) *Re* numbers for $Pr = 4.3$ and $Ra = 7.5 \times 10^9$. The circles (diamonds)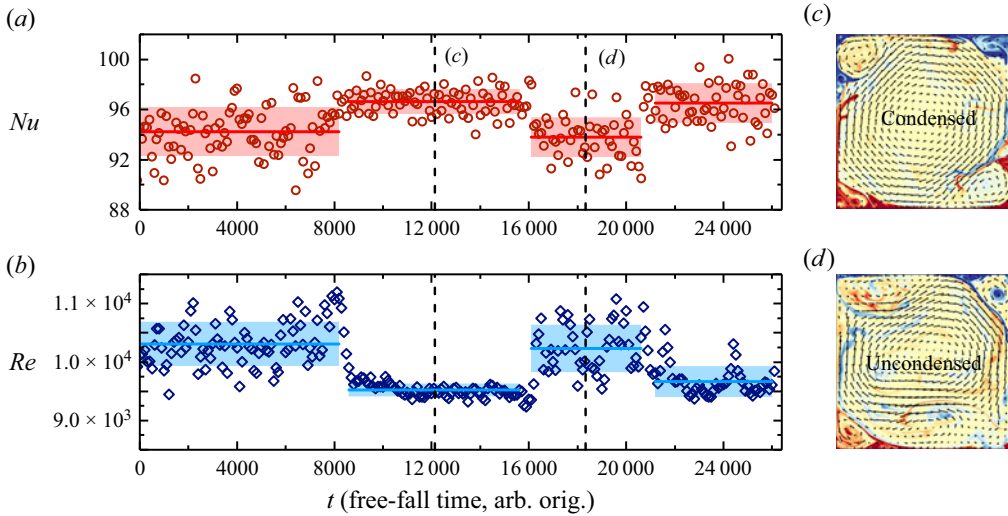 represent the short time-averaged values of *Nu* (*Re*) over 50 free-fall times, corresponding to about five turnover times of the large-scale flow for this case. Four time intervals between successive switching events can be detected in panels (*a*,*b*). The time-averaged and r.m.s.values of *Nu* (*Re*) during each time interval are represented by the red (blue) solid lines and the red (blue) shaded regions, respectively. The instantaneous flow fields at the moments marked by the two dashed lines are shown in panels (*c*,*d*), respectively. The velocity and temperature fields are coded in the same way as figure 4.

relation is also plotted in figure 1, which separates the two flow regimes, i.e. the condensed state and the uncondensed state in the phase diagram.

3.3. *Bistability and the mechanism of the transition*

To understand the scaling relation for Ra_t, we now focus on the flow state in the vicinity of Ra_t to see what happens during the transition. Again we take the cases at $Pr = 4.3$ as examples. By performing long-term simulations, it is found that the flow exhibits a bistability behaviour near Ra_t. This behaviour is characterized by spontaneous switching events between the condensed and uncondensed states, which can be quantified by the Nusselt number *Nu* (dimensionless heat transport) and the Reynolds number *Re* (dimensionless flow strength) as shown in figure 9(*a*,*b*). It is seen that both *Nu* and *Re* exhibit two plateaus with distinct time-averaged and r.m.s.values, and the switching events between the two plateaus in *Nu* and *Re* occur concurrently. Detailed inspection of the flow field indicates that the plateau with higher *Nu* and smaller *Re* corresponds to the condensed state (figure 9*c*), and that with lower *Nu* and larger *Re* corresponds to the uncondensed state (figure 9*d*). The larger r.m.s.values of *Nu* and *Re* for the uncondensed state are also clearly seen, in line with the vigorous energy fluctuations of the Fourier modes. It is worth noting that the lifetimes of the condensed and uncondensed states are comparable for the case shown in figure 9(*a*,*b*), both of which exceed 5000 free-fall times. As the *Ra* number decreases (increases) slightly from $Ra = 7.5 \times 10^9$ to $Ra = 7.15 \times 10^9$ ($Ra = 7.85 \times 10^9$), it is found that the lifetime of the uncondensed (condensed) state decreases to about 1000 free-fall times and the flow becomes dominated by the condensed (uncondensed) state. This sensitive variation trend in lifetimes suggests that the uncondensed (condensed) state will disappear with *Ra* further decreasing

997 A54-11

(increasing) away from Ra_t. In other words, the bistability behaviour exists in a limited Ra number range near Ra_t, as highlighted by open triangles in figure 1. Similar responses of Nu and Re to multiple flow states and the corresponding lifetimes have been reported in previous studies of RBC under different configurations (Xi & Xia 2008; Weiss & Ahlers 2011; van der Poel *et al.* 2012; Xie *et al.* 2018; Zwirner *et al.* 2020; Labarre *et al.* 2023), so we will not discuss this phenomenon further here. What we focus on is how the flow state transition occurs.

Through closely examining the bistability behaviour (see the supplementary movie), it is found that the switching event from the condensed state to the uncondensed case is triggered by some energetic plumes. These plumes, rather than dissipating most of their kinetic energy after travelling across the domain, intrude into the corner rolls when reaching the opposite boundary. As a result, the corner rolls become unstable and detach in the form of orbiting satellite eddies, which release extra thermal energy into the bulk flow and in turn result in more energetic plumes. This chain-reaction-like dynamics maintains the uncondensed state, explaining why the fluctuation is so violent in this state.

The above dynamical process reveals that the flow state transition occurs when the typical time for thermal plumes travelling across the domain $\tau_{pt} \sim H/U$ becomes comparable to their typical dissipative time in the flow $\tau_{\epsilon_u} \sim U^2/\epsilon_u$. In other words, the two time scales are approximately balanced at the edge of the transition. By using the definition of the Re number $Re = UH/\nu$ and the kinetic energy dissipation in the bulk region of the RBC $\epsilon_u = (\nu^3/H^4)NuRaPr^{-2}$ (Lohse & Toschi 2003), the balance of $\tau_{pt} \sim \tau_{\epsilon_u}$ suggests that the critical condition for the transition is given by $Re^3 \sim NuRaPr^{-2}$. Note that the present time-scale balance analysis is a simple dimensional argument, so we have taken the maximum velocity in the flow and the globally averaged kinetic energy dissipation rate as the characteristic properties of thermal plumes, the latter of which is further connected to global responses of the system. This approximation is reasonable in the condensed state, as thermal plumes mostly follow the LSC's motion and primarily determine the global heat transport in this state (Xia *et al.* 2023). By substituting the corresponding scaling relations $Nu \sim Ra^{0.32}Pr^{-0.01}$ and $Re \sim Ra^{0.58}Pr^{-0.87}$ obtained in the condensed state (see figure 11 in the Appendix), we obtain that $Ra_t \sim Pr^{1.43}$, which agrees well with our numerical finding $Ra_t \sim Pr^{1.41}$. The same data analysis has been made in the uncondensed state. The global responses in this state are found to follow $Nu \sim Ra^{0.27}Pr^{0.05}$ and $Re \sim Ra^{0.61}Pr^{-0.94}$ (see figure 11 in the Appendix), leading to a slightly different transition scaling as $Ra_t \sim Pr^{1.55}$. Given the complex dynamics of the main roll and the satellite eddies in the uncondensed state, the discrepancy in the scaling exponents could be attributed to the dramatically different flow states and the uncertainty in estimating the characteristic properties of plumes.

The present phenomenological model can be further generalized to explain the effects of aspect ratio Γ on the transition. For domains with $\Gamma > 1$, because the plume travel distance remains to be the domain's height H, and the Nu and Re numbers depend weakly on Γ (van der Poel *et al.* 2012; Wang *et al.* 2020), so the value of Ra_t is expected to be insensitive to Γ. When $\Gamma < 1$, the flow pattern is featured by vertically stacked rolls (van der Poel *et al.* 2012). For this situation, the plume travel distance can be quantified as ΓH without loss of generality, and then the critical condition for the transition turns out to follow $Re^3 \sim \Gamma NuRaPr^{-2}$. By making use of the data at $Pr = 1$ in the range $0.23 \le \Gamma \le 2/3$ reported by van der Poel *et al.* (2012), which can be described by $Nu \sim \Gamma^{0.34}$ and $Re \sim \Gamma^{0.79}$ roughly (see the Appendix), and assuming that the Ra dependence of Nu and Re remains unchanged, we have $Ra_t \sim \Gamma^{-2.46}$. These predictions

on the Γ dependence of Ra_t are in good agreement with the findings by van der Poel *et al.* (2012) mentioned in the introduction.

4. Summary and concluding remarks

In summary, we have carried out a systematic numerical study of 2-D turbulent RBC in a square domain over the Rayleigh number range $10^7 \leq Ra \leq 2 \times 10^{11}$ and the Prandtl number range $0.25 \leq Pr \leq 20$, aiming to understand a previously noticed but less explored flow state transition. We first show in detail how the flow changes its morphology and dynamics substantially with increasing Ra: from the condensed state characterized by a stable LSC of domain size to the uncondensed state characterized by the emergence of orbiting satellite eddies and irregular wandering motion of the main roll. Then based on a sharp jump in the energy fluctuations of the Fourier modes during the transition, we obtain a scaling relation for the transitional Ra number: $Ra_t = 1.1 \times 10^9 Pr^{1.41}$. Finally, through a close examination of the bistability behaviour near Ra_t, we reveal that the critical condition for the transition is determined by the balance between the travel time of thermal plumes and their dissipation time in the flow, which is supported by our Ra_t-Pr scaling relation. This physical picture also works for the transition observed in 2-D RBC with different aspect ratios (van der Poel *et al.* 2012).

To the best of our knowledge, the flow state transition observed in the present study has not been reported in the studies of both 3-D and quasi-2-D turbulent RBC so far. As discussed in 3.3, one important process during the transition is that the corner rolls become unstable due to the intrusion of some energetic plumes and then detach in the form of satellite eddies. This strong interaction between corner rolls and thermal plumes is enforced by the spatial confinement in 2-D geometry, which can also be achieved by using quasi-2-D configurations. Quasi-2-D RBC shares many similarities in the flow pattern and dynamics with its counterpart in two dimensions (Sugiyama *et al.* 2010; He *et al.* 2021; Li *et al.* 2021), suggesting that a similar flow state transition might occur in quasi-2-D RBC. However, the spatial confinement in quasi-2-D geometry increases the viscous drag on the flow and, thus, the energy dissipation (Chong & Xia 2016; Huang & Xia 2016; Xia *et al.* 2023), which would lead to a higher transitional Ra number according to the present study (similar to the situation of increasing the Pr number). Therefore, to observe a similar flow state transition in quasi-2-D RBC, one should employ a strongly confined convection cell on one hand; but the spatial confinement should not be too severe on the other hand, so that the transitional Ra number is not that high and can be reached by conventional experiments and numerical simulations. It is unknown *a priori* what degree of spatial confinement is appropriate. Some exploratory efforts are on the way and the findings, if any, will be reported in the future.

We end this paper by discussing more on the abrupt change in the energy fluctuations of the Fourier modes during the transition. This signal, together with the bistability behaviour observed in the vicinity of Ra_t, implies that the flow state transition observed here is a phase transition. To confirm this, we adopt an order parameter based on the orientational correlation of the local velocity field to quantify the flow state, which was introduced in the studies of the so-called bacterial turbulence (Cisneros *et al.* 2011; Peng, Liu & Cheng 2021). To be specific, we first calculate the coherence of local velocities by $\phi_{i,local} = \langle \boldsymbol{n}_i \cdot \boldsymbol{n}_j \rangle_{j=1,\ldots,4}$ as illustrated in figure 10(*a*). Here, $\boldsymbol{n}_i \cdot \boldsymbol{n}_j$ stands for the cosine of the angle between adjacent velocity vectors and four neighbours are used for the average. Apparently, $\phi_{i,local} = 1$ represents a perfect-aligned local flow motion and decreasing $\phi_{i,local}$ indicates the velocity field becoming disordered. Thus, the spatiotemporal average
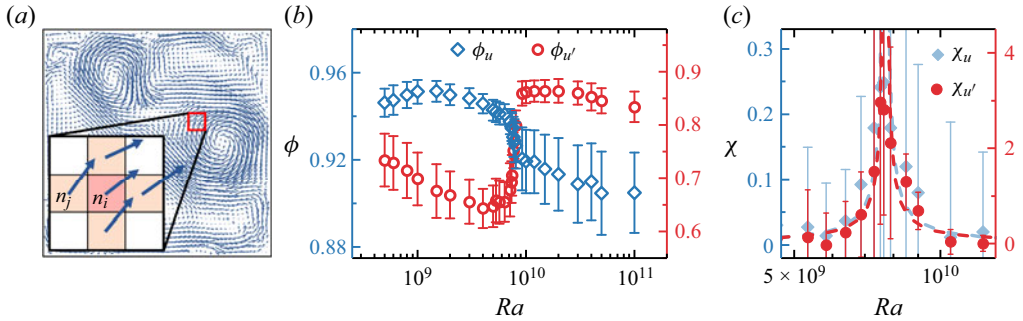
Figure 10. (*a*) Illustration of how to define the orientational correlation $\phi_{i,local}$ from an instantaneous velocity field at $Pr = 4.3$ and $Ra = 1 \times 10^{11}$. (*b*) The order parameter $\phi = \langle \phi_{i,local} \rangle_{V,t}$ of the whole system as a function of Ra at $Pr = 4.3$. Here ϕ_u and $\phi_{u'}$ are obtained from the original and the fluctuating velocity fields, respectively. Panel (*c*) shows $\chi = |\partial \phi / \partial \log(Ra)|$ in the vicinity of the transition. The dashed lines represent data fittings based on the mean field approach: $\chi \propto [\log Ra - \log Ra_t]^{-1}$ with $Ra_t = 7.7 \times 10^9$.

$\phi = \langle \phi_{i,local} \rangle_{V,t}$ represents the global order of the flow. Note that the flow field has been downsampled to a resolution of 48×48 vectors before calculating $\phi_{i,local}$, because neighbouring velocities are naturally aligned when the vector resolution is high. Different sampling densities (ranging from 16×16 to 128×128) have been tested and the results are little affected.

Figure 10(*b*) plots the Ra dependence of the thus-obtained order parameter ϕ. It is seen that the data calculated from the fluctuating velocity field also shows a sharp jump near Ra_t, in line with the behaviour of the energy fluctuations of the Fourier modes. When the system is in the condensed state, the flow field is dominated by the (1,1) and (2,2) modes, whose temporal evolution are relatively gentle. Hence, the order parameter calculated from the fluctuating velocity field is comparatively small. When the flow gets into the uncondensed state, higher-order flow modes characterized by orbiting satellite eddies emerge. Their orbiting motions and interactions with the main roll result in significant temporal evolution in the velocity field. For this flow state, the fluctuating velocity field is dominated by those unsteady eddies (see figure 10*a*), which exhibit stronger spatial correlation and, thus, result in a larger order parameter. The stronger temporal evolution in the flow field also explains why the order parameter obtained from the original velocity field decreases, though slightly, during and after the transition, as the flow structures in the uncondensed state become less organized due to the interaction between multiple vortices. Despite the different variation trends of ϕ_u and $\phi_{u'}$, the absolute values of their gradients $\chi = |\partial \phi / \partial \log(Ra)|$ in the vicinity of transition could be well described by the mean field approach $\chi \propto [\log Ra - \log Ra_t]^{-1}$ (see figure 10*c*). This finding, reminiscent of the classical ferromagnetic phase transition (Pathria & Beale 2011), is striking to see in the present far-from-equilibrium system. A similar result was reported previously in an experimental study of turbulent von Kármán swirling flow (Cortet *et al.* 2010), where the critical exponent for the transition is also 1. In their study, the control parameter is the Re number and the order parameter is defined by the space-averaged angular momentum, which are different from the present study but represent similar physical essences.

While it is unclear to us why the two vastly different flow configurations share the same critical exponent, we propose that the order parameter adopted here could be a unique indicator to quantify the transition behaviours observed in various turbulent flows (e.g. Seshasayanan, Benavides & Alexakis 2014; Benavides & Alexakis 2017; Seshasayanan & Alexakis 2018; van Kan, Nemoto & Alexakis 2019; Musacchio & Boffetta

2019; van Kan & Alexakis 2020; Linkmann, Hohmann & Eckhardt 2020; de Wit *et al.* 2022). Such abrupt transitions between different turbulent flow states have received great interest in recent years (see Alexakis & Biferale (2018) for a review of this topic). It is interesting to see whether these diverse turbulent flows could fall into a universal class in terms of their critical exponents for the transition, which may help to understand the origin of this kind of non-equilibrium phase transition through a unifying framework.

Author ORCIDs.
- Zhen-Yuan Gao https://orcid.org/0009-0004-4727-2529;
- Xin Tao https://orcid.org/0000-0002-7070-0788;
- Shi-Di Huang https://orcid.org/0000-0001-5719-6428;
- Yi-Chao Xie https://orcid.org/0000-0002-2159-4579.

Appendix. Simulation parameters; scaling relations of *Nu* and *Re* numbers

In this appendix, we detail the control parameters and numerical settings used for the present study in table 1. The global response parameters, i.e. the *Nu* and *Re* numbers, are also provided in the table, and their *Ra-Pr* dependent scaling relations are plotted in figures 11(*a*)–11(*d*). Figures 11(*e*, *f*) show the data taken from van der Poel *et al.* (2012). Note that their data at $\Gamma = 0.5$ exhibit some abnormal *Ra*-dependence in the range $10^7 < Ra < 10^9$, the reason of which is unclear to us, so only their data at $Ra = 10^9$ are considered here. The scaling relations obtained in figure 11 are used to estimate the transition scaling exponents for Ra_t in § 3.3.

No.	Pr	Ra	$N_x \times N_z$	Δ_g/η	N_{BL}	N_{BL}^{min}	τ_f	Nu	$Nu_{\epsilon_\theta}(\Lambda_\theta, \%)$	$Nu_{\epsilon_u}(\Lambda_u, \%)$	$Re_{U_{rms}}$	$Re_{U_{max}}$
1	0.25	1.00×10^7	512×576	0.392	34	5	8000	11.14	11.13(−0.1)	11.07(−0.7)	2588	4735
2	0.25	2.00×10^7	512×576	0.504	26	6	7000	14.87	14.85(−0.1)	14.72(−1.0)	3871	7229
3	0.25	5.00×10^7	1024×1152	0.345	49	7	2000	20.41	20.40(−0.0)	20.29(−0.6)	6745	12473
4	0.25	1.00×10^8	1280×1440	0.348	62	8	2000	25.49	25.48(−0.0)	25.33(−0.6)	9312	17888
5	0.25	2.00×10^8	1536×1728	0.360	80	9	1400	30.22	30.21(−0.0)	29.79(−1.4)	15361	33090
6	0.25	5.00×10^8	2048×2304	0.361	93	10	1000	38.37	38.39(0.1)	37.83(−1.4)	24944	57511
7	0.25	8.00×10^8	2048×2304	0.420	84	10	1000	43.87	43.83(−0.1)	42.85(−2.3)	32338	76615
8	0.4	1.00×10^7	512×576	0.313	33	4	8000	11.51	11.50(−0.1)	11.46(−0.4)	1679	3169
9	0.4	2.00×10^7	512×576	0.395	27	5	8000	14.43	14.41(−0.1)	14.34(−0.6)	2518	4768
10	0.4	5.00×10^7	512×576	0.543	20	6	8000	20.19	20.14(−0.2)	19.96(−1.1)	4191	8035
11	0.4	1.00×10^8	1024×1152	0.340	42	6	2000	24.52	24.51(−0.1)	24.41(−0.5)	6275	11773
12	0.4	2.00×10^8	1024×1152	0.432	34	7	1000	31.68	31.66(−0.1)	31.33(−1.1)	8714	17258
13	0.4	5.00×10^8	1280×1440	0.461	42	8	2800	39.95	39.92(−0.1)	39.04(−2.3)	16810	36922
14	0.4	1.00×10^9	1536×1728	0.479	56	8	1400	47.79	47.72(−0.1)	46.49(−2.7)	24187	56365
15	0.4	2.00×10^9	2048×2304	0.449	67	9	1000	58.21	58.12(−0.2)	56.43(−3.1)	35730	85684
16	0.7	1.00×10^7	512×576	0.236	33	3	8000	11.38	11.37(−0.1)	11.35(−0.3)	965	1951
17	0.7	2.00×10^7	512×576	0.298	27	4	8000	14.33	14.31(−0.1)	14.27(−0.4)	1417	2912
18	0.7	5.00×10^7	512×576	0.408	20	4	1000	19.70	19.66(−0.2)	19.56(−0.7)	2398	4970
19	0.7	1.00×10^8	1024×1152	0.259	41	5	2000	25.26	25.25(−0.1)	25.17(−0.4)	3634	7347
20	0.7	2.00×10^8	1024×1152	0.326	34	5	2000	31.49	31.46(−0.1)	31.32(−0.6)	5392	10755
21	0.7	3.00×10^8	1024×1152	0.373	30	5	1600	35.58	35.54(−0.1)	35.38(−0.6)	6776	13501
22	0.7	4.00×10^8	1024×1152	0.410	28	6	1600	39.12	39.05(−0.2)	38.82(−0.7)	8036	15872
23	0.7	5.00×10^8	1024×1152	0.442	26	6	1600	42.11	42.04(−0.2)	41.77(−0.8)	9151	18013
24	0.7	6.10×10^8	1024×1152	0.473	25	6	1200	45.04	44.96(−0.2)	44.62(−0.9)	10499	20263
25	0.7	8.20×10^8	1024×1152	0.516	23	6	1600	47.51	47.39(−0.3)	46.58(−2.0)	13797	29848
26	0.7	1.00×10^9	1024×1152	0.550	22	6	2000	50.26	50.11(−0.3)	49.00(−2.5)	15212	33359
27	0.7	1.50×10^9	1536×1728	0.416	49	7	1200	55.41	55.35(−0.1)	54.54(−1.6)	19246	43514
28	0.7	2.00×10^9	1536×1728	0.457	46	7	1200	60.34	60.22(−0.2)	59.35(−1.6)	22484	51359
29	0.7	3.00×10^9	1536×1728	0.519	42	7	1200	66.91	66.78(−0.2)	65.03(−2.8)	28243	65644
30	0.7	5.00×10^9	2048×2304	0.460	53	8	3000	78.15	78.00(−0.2)	75.05(−4.0)	37078	87853
31	1.2	1.00×10^7	512×576	0.185	40	3	8000	9.12	9.11(−0.1)	9.11(−0.2)	530	1136
32	1.2	2.00×10^7	512×576	0.252	26	3	7000	14.96	14.94(−0.1)	14.91(−0.3)	950	1957

Table 1. For caption see next page.

No.	Pr	Ra	$N_x \times N_z$	Δ_g/η	N_{BL}	N_{BL}^{min}	τ_f	Nu	$Nu_{\epsilon_\theta}(\Lambda_\theta, \%)$	$Nu_{\epsilon_u}(\Lambda_u, \%)$	$Re_{U_{rms}}$	$Re_{U_{max}}$
33	1.2	5.00×10^7	512×576	0.346	19	4	3000	20.73	20.68(−0.2)	20.63(−0.5)	1580	3339
34	1.2	1.00×10^8	512×576	0.433	16	4	3000	25.22	25.13(−0.3)	25.04(−0.7)	2279	4826
35	1.2	2.00×10^8	512×576	0.545	13	4	3000	31.37	31.20(−0.5)	31.06(−1.0)	3326	7020
36	1.2	5.00×10^8	1024×1152	0.368	26	5	1200	41.43	41.35(−0.2)	41.16(−0.7)	5431	11 477
37	1.2	1.00×10^9	1024×1152	0.463	22	5	2000	51.43	51.26(−0.3)	51.04(−0.8)	8445	16 870
38	1.2	2.00×10^9	1280×1440	0.462	29	6	2400	62.33	62.19(−0.2)	61.36(−1.6)	14 423	31 424
39	1.2	5.00×10^9	1536×1728	0.515	36	7	1200	79.04	78.81(−0.3)	77.46(−2.0)	23 914	54 505
40	1.2	1.00×10^{10}	1536×1728	0.643	30	7	1600	96.18	95.71(−0.5)	92.99(−3.3)	34 785	82 679
41	1.2	2.00×10^{10}	2048×2304	0.605	37	8	1000	118.47	118.07(−0.3)	115.72(−2.3)	52 605	126 781
42	2	1.00×10^7	512×576	0.198	33	3	8000	11.48	11.47(−0.1)	11.46(−0.1)	351	763
43	2	2.00×10^7	512×576	0.249	27	3	8000	14.22	14.21(−0.1)	14.19(−0.2)	540	1166
44	2	5.00×10^7	512×576	0.345	19	4	8000	20.56	20.51(−0.2)	20.48(−0.4)	1018	2132
45	2	1.00×10^8	512×576	0.433	16	4	8000	25.17	25.08(−0.3)	25.03(−0.5)	1499	3202
46	2	2.00×10^8	512×576	0.544	13	4	3000	30.99	30.81(−0.6)	30.74(−0.8)	2186	4713
47	2	5.00×10^8	512×576	0.734	10	5	3000	40.79	40.42(−0.9)	40.27(−1.3)	3515	7558
48	2	1.00×10^9	1024×1152	0.460	22	5	1250	50.18	50.01(−0.3)	49.98(−0.4)	5234	10 978
49	2	2.00×10^9	1024×1152	0.579	18	6	1500	62.90	62.63(−0.4)	62.46(−0.7)	8431	16 463
50	2	5.00×10^9	1536×1728	0.519	35	7	1200	81.84	81.54(−0.4)	80.93(−1.1)	15 336	34 084
51	2	8.00×10^9	1536×1728	0.602	32	7	1200	92.41	92.08(−0.4)	90.96(−1.6)	19 502	44 764
52	2	1.00×10^{10}	1536×1728	0.648	30	7	1200	99.17	98.56(−0.6)	97.64(−1.5)	22 417	51 300
53	2	2.00×10^{10}	1536×1728	0.810	25	8	1400	120.36	119.54(−0.7)	117.58(−2.3)	32 875	78 099
54	2	5.00×10^{10}	2048×2304	0.813	29	9	1100	154.60	153.53(−0.7)	148.95(−3.7)	58 260	138 309
55	4.3	2.00×10^7	288×320	0.460	19	3	48 000	16.36	16.29(−0.4)	16.28(−0.5)	281	622
56	4.3	5.00×10^7	288×320	0.617	15	4	12 000	20.92	20.78(−0.7)	20.77(−0.7)	473	1046
57	4.3	8.00×10^7	384×432	0.541	19	4	6000	24.21	24.08(−0.5)	24.07(−0.5)	640	1390
58	4.3	1.00×10^8	384×432	0.582	18	4	6000	25.92	25.78(−0.6)	25.78(−0.6)	730	1581
59	4.3	2.00×10^8	512×576	0.547	13	4	6000	31.70	31.51(−0.6)	31.53(−0.5)	1098	2384
60	4.3	3.00×10^8	1024×1152	0.312	30	4	4000	35.56	35.51(−0.1)	35.50(−0.2)	1388	3044
61	4.3	5.00×10^8	1024×1152	0.368	27	5	8000	41.32	41.23(−0.2)	41.13(−0.5)	1826	4041
62	4.3	6.00×10^8	1024×1152	0.390	25	5	5000	43.60	43.51(−0.2)	43.43(−0.4)	2021	4466
63	4.3	8.00×10^8	1024×1152	0.429	23	5	5000	47.57	47.43(−0.3)	47.32(−0.5)	2368	5213
64	4.3	1.00×10^9	1024×1152	0.461	22	5	3000	50.84	50.66(−0.4)	50.56(−0.6)	2680	5880

Table 1. For caption see next page.

No.	Pr	Ra	$N_x \times N_z$	Δ_g/η	N_{BL}	N_{BL}^{min}	τ_f	Nu	Nu_{ϵ_θ} (Λ_θ, %)	Nu_{ϵ_η} (Λ_u, %)	$Re_{U_{rms}}$	$Re_{U_{max}}$
65	4.3	1.50×10^9	1024×1152	0.527	20	6	3000	57.41	57.17(−0.4)	56.98(−0.7)	3345	7269
66	4.3	2.00×10^9	1024×1152	0.579	18	6	3000	62.69	62.37(−0.5)	62.18(−0.8)	3997	8551
67	4.3	3.00×10^9	1536×1728	0.441	40	6	1500	71.14	70.93(−0.3)	70.72(−0.6)	5168	10713
68	4.3	4.00×10^9	1536×1728	0.485	37	6	1500	78.01	77.76(−0.3)	77.61(−0.5)	6285	12602
69	4.3	5.00×10^9	1536×1728	0.522	34	7	2500	83.75	83.47(−0.3)	83.22(−0.6)	7364	14426
70	4.3	5.30×10^9	1536×1728	0.533	34	7	2000	85.69	85.37(−0.4)	85.23(−0.5)	7713	14969
71	4.3	5.70×10^9	1536×1728	0.547	33	7	2000	88.03	87.64(−0.4)	87.35(−0.8)	8079	15651
72	4.3	6.40×10^9	1536×1728	0.568	32	7	1000	91.36	91.00(−0.4)	90.63(−0.8)	8668	16640
73	4.3	7.15×10^9	1536×1728	0.590	31	7	9500	94.94	94.51(−0.5)	94.03(−1.0)	9585	18143
74	4.3	7.35×10^9	1536×1728	0.595	31	7	10300	95.55	95.14(−0.4)	94.64(−1.0)	9734	18712
75	4.3	7.45×10^9	1536×1728	0.597	31	7	11700	95.86	95.41(−0.5)	94.82(−1.1)	9861	19024
76	4.3	7.50×10^9	1536×1728	0.599	31	7	39500	95.43	95.05(−0.4)	94.19(−1.3)	10023	19403
77	4.3	7.70×10^9	1536×1728	0.603	30	7	6250	96.64	96.20(−0.5)	95.99(−0.7)	10477	20292
78	4.3	7.85×10^9	1536×1728	0.606	30	7	9400	96.62	96.16(−0.5)	95.66(−1.0)	10379	20500
79	4.3	8.10×10^9	1536×1728	0.613	30	7	2750	97.57	97.04(−0.5)	96.69(−0.9)	11054	21654
80	4.3	9.20×10^9	1536×1728	0.636	30	7	2000	99.43	98.99(−0.4)	98.63(−0.8)	11463	24222
81	4.3	1.00×10^{10}	1536×1728	0.652	29	7	1600	101.47	100.87(−0.6)	100.48(−1.0)	11945	25569
82	4.3	1.20×10^{10}	1536×1728	0.691	28	7	1600	106.23	105.72(−0.5)	105.44(−0.7)	13237	28249
83	4.3	1.50×10^{10}	1536×1728	0.743	26	8	1600	113.73	113.03(−0.6)	112.41(−1.2)	14484	32142
84	4.3	2.00×10^{10}	1536×1728	0.814	24	8	1600	123.05	122.16(−0.7)	122.32(−0.6)	16984	38134
85	4.3	3.00×10^{10}	2048×2304	0.695	32	8	2000	138.16	137.42(−0.5)	135.85(−1.7)	20920	48200
86	4.3	4.00×10^{10}	2048×2304	0.761	30	9	1200	148.88	147.77(−0.7)	144.31(−3.1)	25029	58092
87	4.3	5.00×10^{10}	2048×2304	0.820	28	9	1200	160.32	159.02(−0.8)	153.91(−4.0)	27030	64133
88	4.3	1.00×10^{11}	2560×2880	0.874	50	10	1000	194.85	193.23(−0.8)	188.04(−3.5)	40780	98461
89	10	1.00×10^8	512×576	0.443	15	4	8000	27.58	27.45(−0.4)	27.51(−0.3)	337	742
90	10	2.00×10^8	512×576	0.555	12	4	8000	33.55	33.33(−0.7)	33.44(−0.3)	496	1089
91	10	5.00×10^8	512×576	0.745	10	5	8000	43.44	42.95(−1.1)	43.21(−0.5)	846	1824
92	10	1.00×10^9	1024×1152	0.466	21	5	1500	52.75	52.55(−0.4)	52.70(−0.1)	1275	2722
93	10	2.00×10^9	1024×1152	0.584	17	6	1500	64.74	64.33(−0.6)	64.53(−0.3)	1875	3960
94	10	5.00×10^9	1024×1152	0.786	14	7	1500	84.96	84.05(−1.1)	84.66(−0.3)	3256	6819
95	10	1.00×10^{10}	1536×1728	0.657	28	7	3000	104.66	103.99(−0.6)	103.78(−0.8)	4921	10146

Table 1. For caption see next page.

No.	Pr	Ra	$N_x \times N_z$	Δ_g/η	N_{BL}	N_{BL}^{min}	τ_f	Nu	Nu_{ϵ_θ} $(\Lambda_\theta, \%)$	Nu_{ϵ_u} $(\Lambda_u, \%)$	$Re_{U_{rms}}$	$Re_{U_{max}}$
96	10	2.00×10^{10}	2048×2304	0.619	34	8	1750	130.15	129.45(−0.5)	129.38(−0.6)	7745	15 143
97	10	5.00×10^{10}	2048×2304	0.822	28	9	1500	161.45	159.81(−1.0)	160.07(−0.9)	13 602	29 920
98	10	1.00×10^{11}	2560×2880	0.876	49	10	1500	196.89	195.45(−0.7)	195.12(−0.9)	19 633	44 883
99	20	2.00×10^{8}	512×576	0.556	12	4	3000	33.93	33.66(−0.8)	33.82(−0.3)	280	606
100	20	5.00×10^{8}	512×576	0.748	9	5	3000	44.10	43.54(−1.3)	43.90(−0.4)	472	1001
101	20	1.00×10^{9}	1024×1152	0.468	21	5	1500	53.63	53.42(−0.4)	53.62(−0.0)	701	1465
102	20	2.00×10^{9}	1024×1152	0.586	17	6	1500	65.67	65.30(−0.6)	65.63(−0.1)	1038	2128
103	20	5.00×10^{9}	1024×1152	0.788	13	7	1500	85.79	84.84(−1.1)	85.68(−0.1)	1750	3554
104	20	1.00×10^{10}	1536×1728	0.659	28	7	1200	105.49	104.78(−0.7)	105.35(−0.1)	2627	5316
105	20	2.00×10^{10}	2048×2304	0.618	34	8	2500	129.54	128.79(−0.6)	129.26(−0.2)	3936	8075
106	20	3.00×10^{10}	2048×2304	0.706	31	9	2500	146.54	145.45(−0.7)	146.07(−0.3)	5014	10 209
107	20	5.00×10^{10}	2048×2304	0.835	27	9	2500	171.66	169.81(−1.1)	170.96(−0.4)	7022	13 812
108	20	1.00×10^{11}	2560×2880	0.878	49	10	2000	198.93	196.88(−1.0)	197.68(−0.6)	11 116	23 753
109	20	2.00×10^{11}	2560×2880	1.096	41	11	2000	240.88	237.56(−1.4)	234.93(−2.5)	15 898	34 937

Table 1. The numerical details and the global response parameters of the present study. Here Pr and Ra are the control parameters; $N_x \times N_z$ is the spatial resolution; Δ_g is the maximal grid spacing; η represents the Kolmogorov scale estimated by $\eta_K = HPr^{1/2}/[Ra(Nu-1)]^{1/4}$ when $Pr > 1$, or the Bachelor scale estimated by $\eta_B = \eta_K Pr^{-1/2}$ when $Pr \leq 1$; N_{BL} is the number of grid points used for the boundary layer and N_{BL}^{min} is the required minimum number according to Shishkina *et al.* (2010); τ_f is the time duration (in units of free-fall time) to get statistics; Nu, Nu_{ϵ_θ} and Nu_{ϵ_u} are the dimensionless heat transfer efficiency obtained through the definition, the thermal and the kinetic dissipation rates, respectively; Λ_θ (Λ_u) is the relative error between Nu and Nu_{ϵ_θ} (Nu_{ϵ_u}); $Re_{U_{rms}}$ and $Re_{U_{max}}$ are the Reynolds numbers characterized by different velocities U, where $U_{rms} = \sqrt{\langle u^2 + w^2 \rangle_{V,t}}$ and $U_{max} = \langle \max\{U\} \rangle_t$.
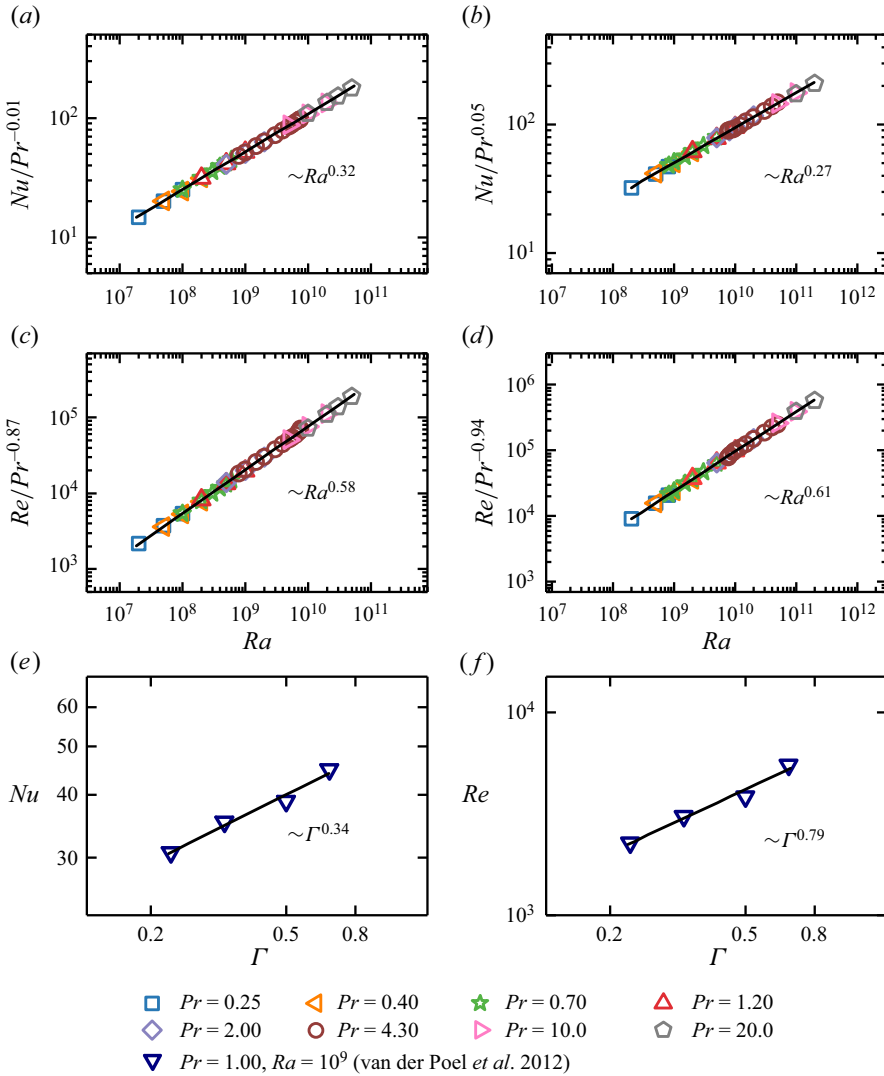
Figure 11. The compensated Nu and Re as a function of Ra for each Pr obtained in the present study: panels (a,c) show the results in the condensed state and (b,d) are in the uncondensed state. Solid lines are the corresponding least-square fits, which yield $Nu \sim Ra^{0.32}Pr^{-0.01}$, $Re \sim Ra^{0.58}Pr^{-0.87}$ and $Nu \sim Ra^{0.27}Pr^{0.05}$, $Re \sim Ra^{0.61}Pr^{-0.94}$ for the condensed and uncondensed states, respectively. Since there exists no simple scaling law over a wide Ra range (Grossmann & Lohse 2000), only the data one decade before or after Ra_t are used to get the effective scaling exponents. Panels (e,f) show the Γ dependencies of Nu and Re, respectively. The data are taken from figure 2 of van der Poel *et al.* (2012), and the least-square power law fitting yields $Nu \sim \Gamma^{0.34}$ and $Re \sim \Gamma^{0.79}$ roughly.

References

AHLERS, G., GROSSMANN, S. & LOHSE, D. 2009 Heat transfer and large scale dynamics in turbulent Rayleigh–Bénard convection. *Rev. Mod. Phys.* **81**, 503–537.

ALEXAKIS, A. & BIFERALE, L. 2018 Cascades and transitions in turbulent flows. *Phys. Rep.* **767–769**, 1–101.

BAO, Y., CHEN, J., LIU, B.-F., SHE, Z.-S., ZHANG, J. & ZHOU, Q. 2015 Enhanced heat transport in partitioned thermal convection. *J. Fluid Mech.* **784**, R5.

BAO, Y., LUO, J. & YE, M. 2018 Parallel direct method of DNS for two-dimensional turbulent Rayleigh–Bénard convection. *J. Mech.* **34**, 159–166.

BENAVIDES, S.J. & ALEXAKIS, A. 2017 Critical transitions in thin layer turbulence. *J. Fluid Mech.* **822**, 364–385.

BOUCHET, F. & SIMONNET, E. 2009 Random changes of flow topology in two-dimensional and geophysical turbulence. *Phys. Rev. Lett.* **102**, 094504.

BRENT, A.D., VOLLER, V.R. & REID, K.J. 1988 Enthalpy-porosity technique for modeling convection-diffusion phase change: application to the melting of a pure metal. *Numer. Heat Transfer* **13**, 297–318.

BROWN, E. & AHLERS, G. 2006 Rotations and cessations of the large-scale circulation in turbulent Rayleigh–Bénard convection. *J. Fluid Mech.* **568**, 351–386.

BROWN, E., NIKOLAENKO, A. & AHLERS, G. 2005 Reorientation of the large-scale circulation in turbulent Rayleigh–Bénard convection. *Phys. Rev. Lett.* **95**, 084503.

CASTILLO-CASTELLANOS, A., SERGENT, A., PODVIN, B. & ROSSI, M. 2019 Cessation and reversals of large-scale structures in square Rayleigh–Bénard cells. *J. Fluid Mech.* **877**, 922–954.

CATTANEO, F., EMONET, T. & WEISS, N. 2003 On the interaction between convection and magnetic fields. *Astrophys. J.* **588**, 1183–1198.

CHANDRA, M. & VERMA, M.K. 2011 Dynamics and symmetries of flow reversals in turbulent convection. *Phys. Rev.* E **83**, 067303.

CHEN, X., HUANG, S.-D., XIA, K.-Q. & XI, H.-D. 2019 Emergence of substructures inside the large-scale circulation induces transition in flow reversals in turbulent thermal convection. *J. Fluid Mech.* **877**, R1.

CHEN, X.-Y., XIE, Y.-C., YANG, J.-C. & NI, M.-J. 2023 Strong coupling of flow structure and heat transport in liquid metal thermal convection. *J. Fluid Mech.* **975**, A21.

CHILLÀ, F. & SCHUMACHER, J. 2012 New perspectives in turbulent Rayleigh–Bénard convection. *Eur. Phys. J.* E **35**, 1–25.

CHONG, K.L. & XIA, K.-Q. 2016 Exploring the severely confined regime in Rayleigh–Bénard convection. *J. Fluid Mech.* **805**, R4.

CILIBERTO, S., CIONI, S. & LAROCHE, C. 1996 Large-scale flow properties of turbulent thermal convection. *Phys. Rev.* E **54**, R5901.

CISNEROS, L.H., KESSLER, J.O., GANGULY, S. & GOLDSTEIN, R.E. 2011 Dynamics of swimming bacteria: transition to directional order at high concentration. *Phys. Rev.* E **83**, 061907.

CORTET, P.-P., CHIFFAUDEL, A., DAVIAUD, F. & DUBRULLE, B. 2010 Experimental evidence of a phase transition in a closed turbulent flow. *Phys. Rev. Lett.* **105**, 214501.

FAVIER, B., GUERVILLY, C. & KNOBLOCH, E. 2019 Subcritical turbulent condensate in rapidly rotating Rayleigh–Bénard convection. *J. Fluid Mech.* **864**, R1.

FUNFSCHILLING, D., BROWN, E. & AHLERS, G. 2008 Torsional oscillations of the large-scale circulation in turbulent Rayleigh–Bénard convection. *J. Fluid Mech.* **607**, 119–139.

GROSSMANN, G. & LOHSE, D. 2000 Scaling in thermal convection: a unifying theory. *J. Fluid Mech.* **407**, 27–56.

GROSSMANN, S. & LOHSE, D. 2001 Thermal convection for large Prandtl numbers. *Phys. Rev. Lett.* **86**, 3316.

HARTMANN, D.L., MOY, L.A. & FU, Q. 2001 Tropical convection and the energy balance at the top of the atmosphere. *J. Clim.* **14**, 4495–4511.

HE, J.-C, BAO, Y. & CHEN, X. 2023 Scaling transition of thermal dissipation in turbulent convection. *Phys. Fluids* **35**, 015126.

HE, J.-C., FANG, M.-W., GAO, Z.-Y., HUANG, S.-D. & BAO, Y. 2021 Effects of Prandtl number in two-dimentional turbulent convection. *Chin. Phys.* B **30**, 094701.

HUANG, S.-D. & XIA, K.-Q. 2016 Effects of geometric confinement in quasi-2-D turbulent Rayleigh–Bénard convection. *J. Fluid Mech.* **794**, 639–654.

HUANG, Y.-X. & ZHOU, Q. 2013 Counter-gradient heat transport in two-dimensional turbulent Rayleigh–Bénard convection. *J. Fluid Mech.* **737**, R3.

HUISMAN, S.G., VAN DER VEEN, R.C.A., SUN, C. & LOHSE, D. 2014 Multiple states in highly turbulent Taylor–Couette flow. *Nat. Commun.* **5**, 3820.

VAN KAN, A. & ALEXAKIS, A. 2020 Critical transition in fast-rotating turbulence within highly elongated domains. *J. Fluid Mech.* **899**, A33.

VAN KAN, A., NEMOTO, T. & ALEXAKIS, A. 2019 Rare transitions to thin-layer turbulent condensates. *J. Fluid Mech.* **878**, 356–369.

KRAICHNAN, R.H. 1967 Inertial ranges in two-dimensional turbulence. *Phys. Fluids* **10**, 1417–1423.

LABARRE, V., FAUVE, S. & CHIBBARO, S. 2023 Heat-flux fluctuations revealing regime transitions in Rayleigh–Bénard convection. *Phys. Rev. Fluids* **8**, 053501.

LANDAU, L.D. & LIFSHITZ, E.M. 1987 *Fluid Mechanics*. Pergamon.

LI, X.-M., HE, J.-D., TIAN, Y., HAO, P. & HUANG, S.-D. 2021 Effects of Prandtl number in quasi-two-dimensional Rayleigh–Bénard convection. *J. Fluid Mech.* **915**, A60.

LI, Y.-Z., CHEN, X., XU, A. & XI, H.-D. 2022 Counter-flow orbiting of the vortex centre in turbulent thermal convection. *J. Fluid Mech.* **935**, A19.

LINDBORG, E. 2023 Reynolds-number scaling and convergence time scale in two-dimensional Rayleigh–Bénard convection. *J. Fluid Mech.* **973**, A9.

LINKMANN, M., HOHMANN, M. & ECKHARDT, B. 2020 Non-universal transitions to two-dimensional turbulence. *J. Fluid Mech.* **892**, A18.

LOHSE, D. & TOSCHI, F. 2003 Ultimate state of thermal convection. *Phys. Rev. Lett.* **90**, 034502.

LOHSE, D. & XIA, K.-Q. 2010 Small-scale properties of turbulent Rayleigh–Bénard convection. *Annu. Rev. Fluid Mech.* **42**, 335–364.

MUSACCHIO, S. & BOFFETTA, G. 2019 Condensate in quasi-two-dimensional turbulence. *Phys. Rev. Fluids* **4**, 022602.

PANDEY, A. 2021 Thermal boundary layer structure in low-Prandtl-number turbulent convection. *J. Fluid Mech.* **910**, A13.

PATHRIA, R.K. & BEALE, P.D. 2011 *Statistical Mechanics*. Elsevier.

PENG, Y., LIU, Z.Y. & CHENG, X. 2021 Imaging the emergence of bacterial turbulence: phase diagram and transition kinetics. *Sci. Adv.* **7**, eabd1240.

PODVIN, B. & SERGENT, A. 2015 A large-scale investigation of wind reversal in a square Rayleigh–Bénard cell. *J. Fluid Mech.* **766**, 172–201.

VAN DER POEL, E.P., OSTILLA-MÓNICO, R., VERZICCO, R., GROSSMANN, S. & LOHSE, D. 2015 Logarithmic mean temperature profiles and their connection to plume emissions in turbulent Rayleigh–Bénard convection. *Phys. Rev. Lett.* **115**, 154501.

VAN DER POEL, E.P., STEVENS, R.J.A.M. & LOHSE, D. 2011 Connecting flow structures and heat flux in turbulent Rayleigh–Bénard convection. *Phys. Rev.* E **84**, 045303.

VAN DER POEL, E.P., STEVENS, R.J.A.M. & LOHSE, D. 2013 Comparison between two- and three-dimensional Rayleigh–Bénard convection. *J. Fluid Mech.* **736**, 177–194.

VAN DER POEL, E.P., STEVENS, R.J.A.M., SUGIYAMA, K. & LOHSE, D. 2012 Flow states in two-dimensional Rayleigh–Bénard convection as a function of aspect-ratio and Rayleigh number. *Phys. Fluids* **24**, 085104.

QIU, X.-L., YAO, S.H. & TONG, P. 2000 Large-scale coherent rotation and oscillation in turbulent thermal convection. *Phys. Rev.* E **61**, R6075–R6078.

REN, L., TAO, X., ZHANG, L., NI, M.-J., XIA, K.-Q. & XIE, Y.-C. 2022 Flow states and heat transport in liquid metal convection. *J. Fluid Mech.* **951**, R1.

SAMUEL, R. & VERMA, M.K. 2024 Bolgiano–Obukhov scaling in two-dimensional Rayleigh–Bénard convection at extreme Rayleigh numbers. *Phys. Rev. Fluids* **9**, 023502.

SCHMALZL, J., BREUER, M. & HANSEN, U. 2004 On the validity of two-dimensional numerical approaches to time-dependent thermal convection. *Europhys. Lett.* **67**, 390.

SESHASAYANAN, K. & ALEXAKIS, A. 2018 Condensates in rotating turbulent flows. *J. Fluid Mech.* **841**, 434–462.

SESHASAYANAN, K., BENAVIDES, S.J. & ALEXAKIS, A. 2014 On the edge of an inverse cascade. *Phys. Rev.* E **90**, 051003.

SHISHKINA, O., STEVENS, R.J.A.M., GROSSMANN, S. & LOHSE, D. 2010 Boundary layer structure in turbulent thermal convection and its consequences for required numerical resolution. *New J. Phys.* **12**, 075022.

STEVENS, R.J.A.M., VAN DER POEL, E.P, GROSSMANN, S. & LOHSE, D. 2013 The unifying theory of scaling in thermal convection: the updated prefactors. *J. Fluid Mech.* **730**, 295–308.

SUGIYAMA, K., CALZAVARINI, E., GROSSMANN, S. & LOHSE, D. 2009 Flow organization in two-dimensional non-Oberbeck–Boussinesq Rayleigh–Bénard convection in water. *J. Fluid Mech.* **637**, 105–135.

SUGIYAMA, K., NI, R., STEVENS, R.J.A.M., CHAN, T.-S., ZHOU, S.-Q., XI, H.-D., SUN, C., GROSSMANN, S., XIA, K.-Q. & LOHSE, D. 2010 Flow reversals in thermally driven turbulence. *Phys. Rev. Lett.* **105**, 034503.

VOGT, T., HORN, S., GRANNAN, A.M. & AURNOU, J.M. 2018 Jump rope vortex in liquid metal convection. *Proc. Natl Acad. Sci. USA* **115**, 12674–12679.

WANG, Q., VERZICCO, R., LOHSE, D. & SHISHKINA, O. 2020 Multiple states in turbulent large-aspect-ratio thermal convection: what determines the number of convection rolls. *Phys. Rev. Lett.* **125**, 074501.

WANG, Q., XIA, S.-N., WANG, B.-F., SUN, D.-J., ZHOU, Q. & WAN, Z.-H. 2018 Flow reversals in two-dimensional thermal convection in tilted cells. *J. Fluid Mech.* **849**, 355–372.

WEEKS, E.R., TIAN, Y., URBACH, J.S., IDE, K., SWINNEY, H.L. & GHIL, M. 1997 Transitions between blocked and zonal flows in a rotating annulus with topography. *Science* **278**, 1598–1601.

WEI, P. 2021 The persistence of large-scale circulation in Rayleigh–Bénard convection. *J. Fluid Mech.* **924**, A28.

WEISS, S. & AHLERS, G. 2011 Turbulent Rayleigh–Bénard convection in a cylindrical container with aspect ratio $\Gamma = 0.50$ and Prandtl number $Pr = 4.38$. *J. Fluid Mech.* **676**, 5–40.

DE WIT, X.M., AGUIRRE GUZMÁN, A.J., CLERCX, H.J.H. & KUNNEN, R.P.J. 2022 Discontinuous transitions towards vortex condensates in buoyancy-driven rotating turbulence. *J. Fluid Mech.* **936**, A43.

XI, H.-D., LAM, S. & XIA, K.-Q. 2004 From laminar plumes to organized flows: the onset of large-scale circulation in turbulent thermal convection. *J. Fluid Mech.* **503**, 47–56.

XI, H.-D. & XIA, K.-Q. 2007 Cessations and reversals of the large-scale circulation in turbulent thermal convection. *Phys. Rev.* E **75**, 066307.

XI, H.-D. & XIA, K.-Q. 2008 Flow mode transitions in turbulent thermal convection. *Phys. Fluids* **20**, 055104.

XI, H.-D, ZHOU, S.-Q., ZHOU, Q., CHAN, T.-S. & XIA, K.-Q. 2009 Origin of the temperature oscillation in turbulent thermal convection. *Phys. Rev. Lett.* **102**, 044503.

XIA, H., BYRNE, D., FALKOVICH, G. & SHATS, M. 2011 Upscale energy transfer in thick turbulent fluid layers. *Nat. Phys.* **7**, 321–324.

XIA, K.-Q. 2013 Current trends and future directions in turbulent thermal convection. *Theor. Appl. Mech. Lett.* **3**, 052001.

XIA, K.-Q., HUANG, S.-D., XIE, Y.-C. & ZHANG, L. 2023 Tuning heat transport via coherent structure manipulation: recent advances in thermal turbulence. *Natl Sci. Rev.* **10**, nwad012.

XIE, J.-H. & HUANG, S.-D. 2022 Bolgiano–Obukhov scaling in two-dimensional isotropic convection. *J. Fluid Mech.* **942**, A19.

XIE, Y.-C., DING, G.-Y. & XIA, K.-Q. 2018 Flow topology transition via global bifurcation in thermally driven turbulence. *Phys. Rev. Lett.* **120**, 214501.

XIE, Y.-C., WEI, P. & XIA, K.-Q. 2013 Dynamics of the large-scale circulation in high-Prandtl-number turbulent thermal convection. *J. Fluid Mech.* **717**, 322–346.

XU, A., CHEN, X. & XI, H.-D. 2021 Tristable flow states and reversal of the large-scale circulation in two-dimensional circular convection cells. *J. Fluid Mech.* **910**, A33.

YANAGISAWA, T., YAMAGISHI, Y., HAMANO, Y., TASAKA, Y., YOSHIDA, M., YANO, K. & TAKEDA, Y. 2010 Structure of large-scale flows and their oscillation in the thermal convection of liquid gallium. *Phys. Rev.* E **82**, 016320.

YANG, Y., CHEN, W., VERZICCO, R. & LOHSE, D. 2020 Multiple states and transport properties of double-diffusive convection turbulence. *Proc. Natl Acad. Sci. USA* **117**, 14676–14681.

ZHANG, Y. & ZHOU, Q. 2024 Low-Prandtl-number effects on global and local statistics in two-dimensional Rayleigh–Bénard convection. *Phys. Fluids* **36**, 015107.

ZHANG, Y., ZHOU, Q. & SUN, C. 2017 Statistics of kinetic and thermal energy dissipation rates in two-dimensional turbulent Rayleigh–Bénard convection. *J. Fluid Mech.* **814**, 165–184.

ZHOU, Q., STEVENS, R.J.A.M., SUGIYAMA, K., GROSSMANN, S., LOHSE, D. & XIA, K.-Q. 2010 Prandtl–Blasius temperature and velocity boundary-layer profiles in turbulent Rayleigh–Bénard convection. *J. Fluid Mech.* **664**, 297–312.

ZHOU, Q., XI, H.-D., ZHOU, S.-Q., SUN, C. & XIA, K.-Q. 2009 Oscillations of the large-scale circulation in turbulent Rayleigh–Bénard convection: the sloshing mode and its relationship with the torsional mode. *J. Fluid Mech.* **630**, 367–390.

ZHU, X., MATHAI, V., STEVENS, R.J.A.M., VERZICCO, R. & LOHSE, D. 2018 Transition to the ultimate regime in two-dimensional Rayleigh–Bénard convection. *Phys. Rev. Lett.* **120**, 144502.

ZWIRNER, L., TILGNER, A. & SHISHKINA, O. 2020 Elliptical instability and multiple-roll flow modes of the large-scale circulation in confined turbulent Rayleigh–Bénard convection. *Phys. Rev. Lett.* **125**, 054502.